Contract No. and Disclaimer:

Four Pi Calibration and Modeling of a Bare Germanium Detector in a Cylindrical Field Source

R. A. Dewberry and J. E. Young
Savanah River National Laboratory
Aiken, SC 29808
USA

Introduction

In reference 1 the authors described γ-ray holdup assay of a Mossbauer spectroscopy instrument where they utilized two axial symmetric cylindrical shell acquisitions and two disk source acquisitions to determine Am-241 and Np-237 contamination. The measured contents of the two species were determined using a general detector efficiency calibration taken from a 12-inch point source.[2] The authors corrected the raw spectra for container absorption as well as for geometry corrections to transform the calibration curve to the applicable axial symmetric cylindrical source- and disk source- of contamination. The authors derived the geometry corrections with exact calculus that are shown in equations (1) and (2) of our **Experimental** section.

A cylindrical shell (oven source) acquisition configuration is described in reference 3, where the authors disclosed this configuration to gain improved sensitivity for holdup measure of U-235 in a ten-chamber oven. The oven was a piece of process equipment used in the Savannah River Plant M-Area Uranium Fuel Fabrication plant for which a U-235 holdup measurement was necessary for its decontamination and decommissioning in 2003.[4] In reference 4 the authors calibrated a bare NaI detector for these U-235 holdup measurements. In references 5 and 6 the authors calibrated a bare HpGe detector in a cylindrical shell configuration for improved sensitivity measurements of U-235 in other M-Area process equipment. Sensitivity was vastly improved compared to a close field view of the sample, with detection efficiency of greater than 1% for the 185.7-keV γ-ray from U-235.

In none of references 3 - 7 did the authors resolve the exact calculus descriptions of the acquisition configurations. Only the empirical efficiency for detection of the 185.7-keV photon from U-235 decay was obtained. Not until the 2010 paper of reference 1 did the authors derive a good theoretical description of the flux of photons onto the front face of a detector from an axially symmetric cylindrical shell. Subsequent to publication of 1, the theoretical treatment of the cylindrical shell and disk source acquisition sources was recognized by the Los Alamos National Laboratory as suitable for including in the Safeguards Training Program.[8] Therefore, we felt it was important to accurately demonstrate the calculus describing the cylindrical shell configuration for the HpGe detector and to theoretically account for the observed bare-detector efficiencies measured in references (3 – 6).

In this paper we demonstrate the applicability of the cylindrical shell derivation to a flexible planar sheet of known Am-241, Eu-152, and Cs-137 activity that we rolled into a symmetrical cylindrical shell of radioactivity. Using the geometry correction equation of

reference 1, we calculate geometry correction values using the known detector and source dimensions combined with source to detector distances. We then compare measured detection efficiencies from a cylindrical shell of activity for the 185.7-keV photon (U-235) and for the 414.3-keV photon (Pu-239) with those determined for a 12-inch point source[2,7] to demonstrate agreement between experiment and the theoretically calculated values derived by the Savannah River National Laboratory (SRNL) authors of reference 1. We demonstrate this geometry correction first for the 185.7- and 414.3-keV γ-rays. But because the detector was point source calibrated at 12 inches for the energy range (60 - 1700) keV (using two distinct sources) to map its intrinsic efficiency, the *geometry* correction for any acquisition configuration holds for all photon energies.[2] We demonstrate that for ten photon energies in the range 121 keV to 967 keV.

The good agreement between experiment and calculation is demonstrated at five source to detector distances using the identical shielded HpGe detector of references 4 – 7 as well as with a separate HpGe detector. We then extend the measurement to include a single acquisition where the flexible source is wrapped around the bare detector in a symmetrical cylinder that radiates on both faces of the detector as well as on to the detector's cylindrical sides of known dimensions. We derive the exact calculus to calculate the flux of the source on to the cylindrical sides of the detector. We then demonstrate outstanding agreement between the measured efficiency for the two primary U-235 and Pu-239 photons in this *oven* source configuration compared to the point source of activity for which the detector was originally calibrated.

Experimental

To obtain the cylindrical shell acquisition efficiencies, we set up the identical HpGe detector used in references 2 – 7 and used the identical ½ inch Pb cylindrical shield to view an axially symmetric cylinder of radioactivity at two distances. The cylindrical source was made up from our flexible uniform planar source[9] with dimensions 9.625 inches by 19.75 inches, and with known radioactive contents 7.163×10^5 dps Eu-152, 4.357×10^5 dps Cs-137, and 5.853×10^5 dps Am-241 dated 13 June 1995.

The flexible source was rolled to make a uniform cylinder of activity with radius 3.125 inch ($19.75/2\pi$) and length (height) 9.625 inches. The source was set up so that the HpGe detector was able to view it down the symmetrical axis of radius 3.125 inches at our selected source to detector distances. This then defined our cylindrical shell configuration from which we were able to make measurements for comparing with the theory of equation (1).

In reference 1 the authors derived the flux of activity reaching the face of a cylindrical detector to be defined by

$$\Phi(A) = -[S_{area}/4\pi]\int_{\theta}\int_{\phi}\cos\theta d\theta d\phi. \qquad (1)$$

$$= -[S_{area}/4\pi]\int_{\phi}[\sin(\theta_2) - \sin(\theta_1)]d\phi \quad = \; 0.5[\sin(\theta_2) - \sin(\theta_1)]S_{area}.$$

The extremes θ_2 and θ_1 are determined by the height of the cylindrical source and the source to detector distance as shown in Figure 1.

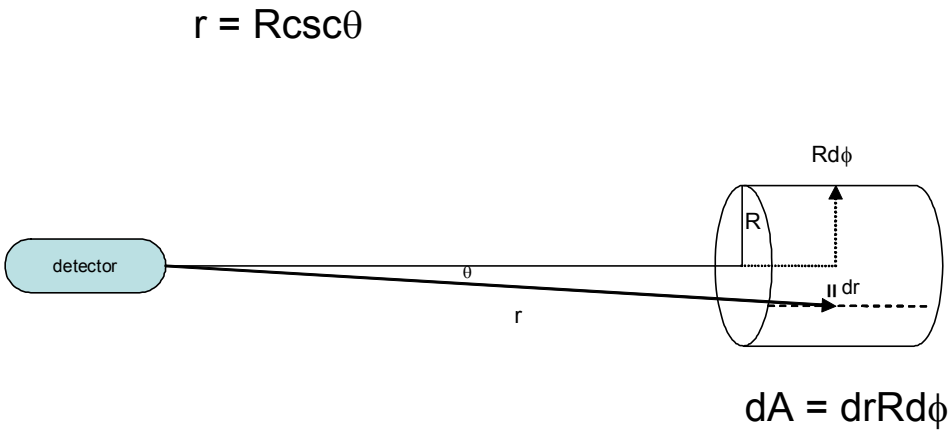

Figure 1. Schematic view of cylindrical acquisition configuration showing r(θ), dr and dA.

And the flux of activity of a disk source reaching the detector face was derived to be

$$\Phi(A) = [S_{disk}/4][\ln(1 + R^2/x^2)], \qquad (2)$$

as depicted in Figure 2.

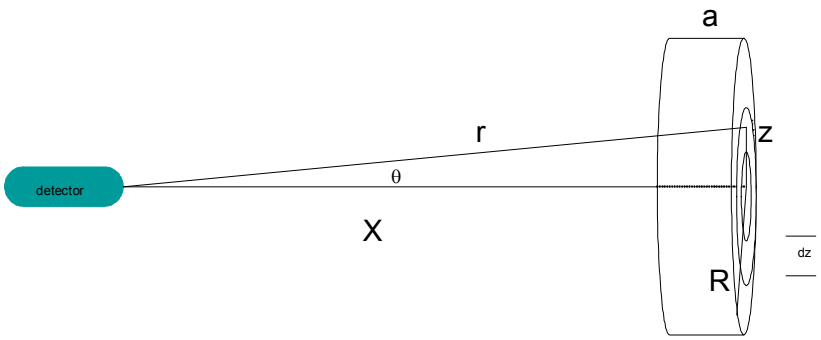

Figure 2. Schematic view of an axial acquisition of a disk.

We test the results of (1) using five source to detector distances of 12 inches to 29 inches. Once again the source height is 9.625 inches. For most of this paper we perform our calculations in the centimeter-gram-second system of units, so the cylinder height is 24.45 cm. The detector is a cylindrical right prism of radius 2.74 cm and height 3.53 cm.[10]

The HpGe detector was calibrated in the point source acquisition configuration in both references 2 and 7. In reference 7 the detector was shown to have a point source calibration constant of $K_p = 2.36 \times 10^{-5}$ g-sec/cm^2 for the 185.7-keV photon of U-235. For a 12-inch point source this yields a detection efficiency of

$$[1 \text{ g U-235}] = K_p(d)^2 \text{cps}, \qquad (3)$$

where cps is the measured detection rate of the 185.7-keV photon of a 1-g source at 12 inches. Thus

$$\text{cps} = 1/(2.36 \times 10^{-5})(12*12)(2.54*2.54) = 45.6 \text{ cps.}$$

A 1-g source of U-235 contains

$$(\text{SpA})\text{branch} = (2.14\text{x}10^{-6} \text{ Ci})(3.7\text{x}10^{10})(0.53) = 42000 \text{ dps}$$

of activity in the 185.7-keV photon, yielding a detection efficiency of 0.00109. This is in good agreement with the experimental 12-inch point source efficiency equation of Sigg for this detector

$$LN(Eff) = -536.73072 + 422.79636 * LN(E) - 134.01688 * LN(E)^2 + 21.13637 * LN(E)^3 - 1.66165 * LN(E)^4 + 0.05208 * LN(E)^5, \quad (4)$$

where E is the gamma-ray energy in keV, and
Eff is the detector efficiency at energy E.

This equation yields the 12-inch point source curve of Figure 3. From it we observe the detection efficiencies of 0.000905 for the 185.7 keV photon of U-235 (good agreement with reference 7), and 0.000474 for the 414-keV photon of Pu-239. For further comparisons using the 2000 data we use the experimental equation of Sigg.

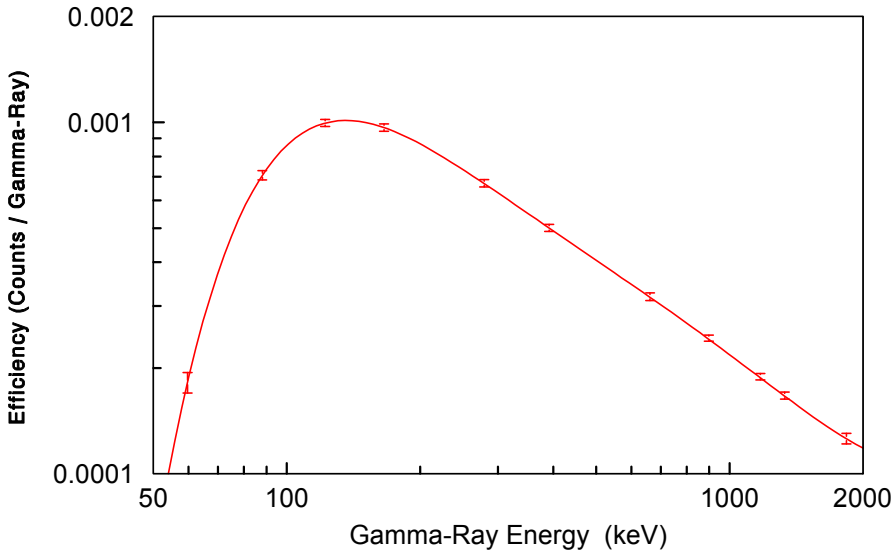

Figure 3. Experimental 12-inch point source detection efficiency of the HpGe detector described in text as m-det S/N 38-TP31258A.

In Figure 4 we show a photograph of a cylindrical shell acquisition using our flexible planar source wrapped into a cylinder of R = 3.125 inches and height 9.625 inches. We obtained acquisitions at 12 inches and 20 inches from the detector face in order to test the flux onto the face of the detector calculated by equation (1). We then repeated using the same flexible planar source and using a second detector (mrs-det S/N 36-TP210858B) that had also been efficiency calibrated in the 12-inch point source configuration.[11,12] We acquired cylindrical shell data at distances of 13 inches, 23 inches, and 29 inches with this detector. To reconfirm the source attributes, we obtained a single acquisition with this second detector viewing the planar source as a flat plane perpendicular to the detector axis at a distance of 84 inches.[13] We could model the source very accurately as a plane using the analysis code ISOTOPIC[(12)], but at that distance it appears very nearly as a point source. We do not present results of that confirmatory measurement.

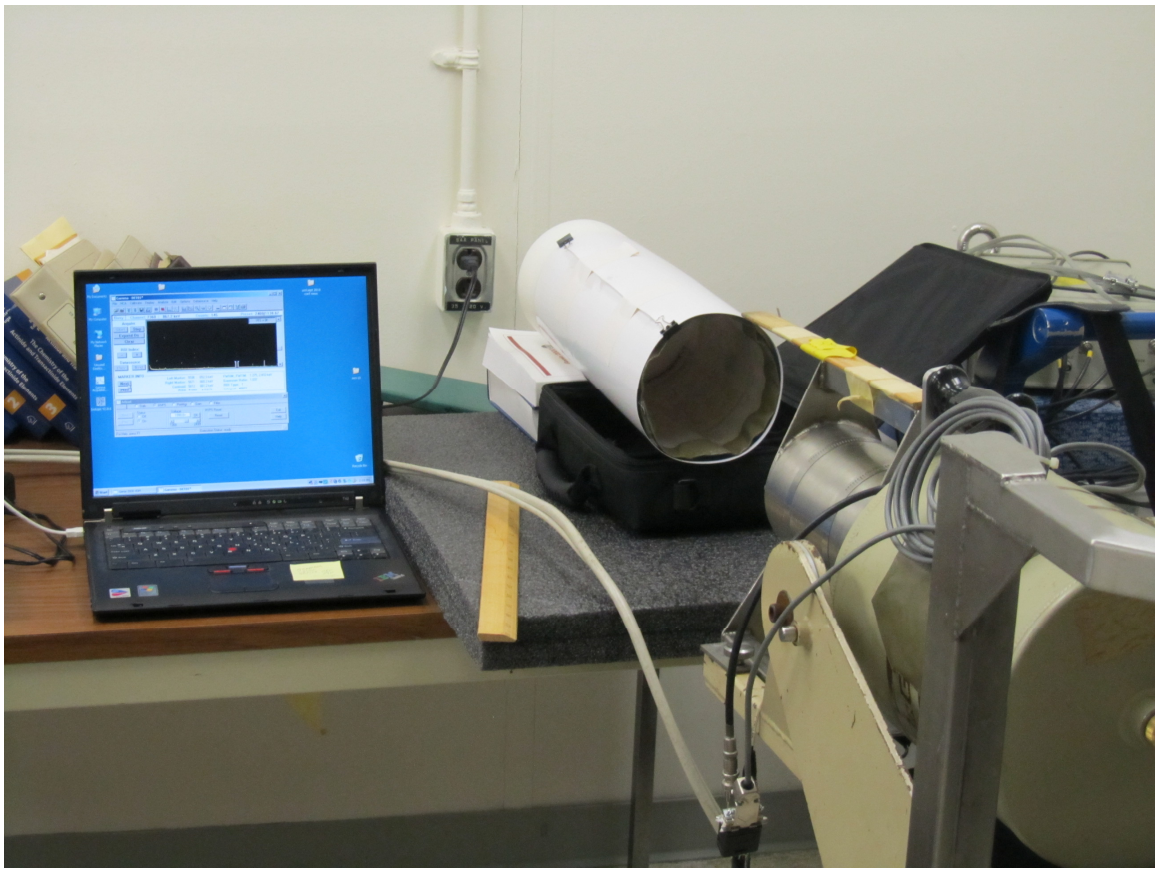

Figure 4. Photograph of the detector viewing down the axis of the cylindrical source.

We finally use the cylindrical shell calibration obtained in June 2000 on the bare HpGe detector to reconcile the observed efficiency of both the primary U-235 and Pu-239 photons. This efficiency measurement was performed by wrapping the flexible source inside a critically safe uranium storage container that had an inside diameter of 6.25 inches. (It was extremely fortuitous that the process components of reference 5 and 6 had this inside diameter, so that the available flexible planar source made almost exactly one complete wrap around the inside.) We placed the bare HpGe detector inside the container as sketched in Figure 5.

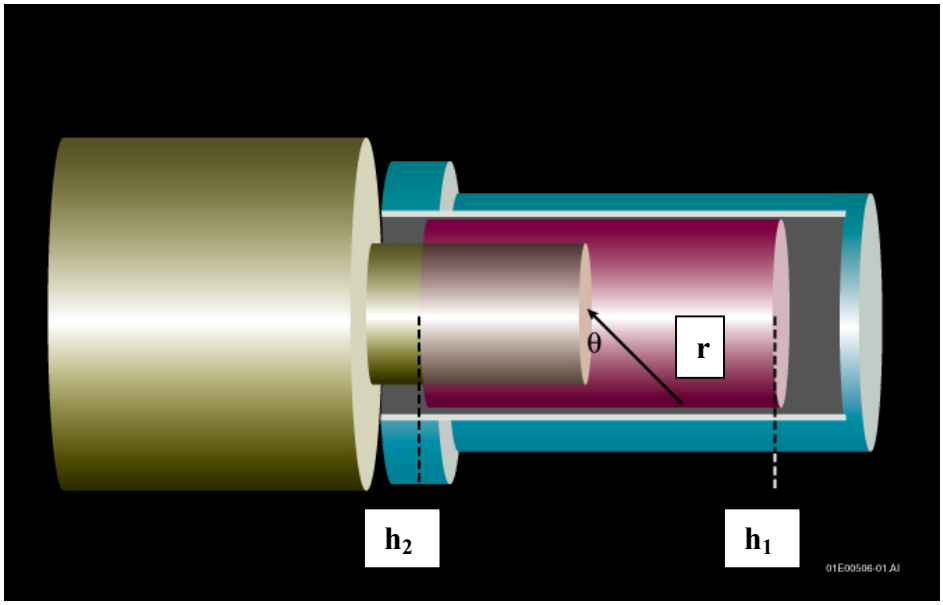

Figure 5. Cylindrical source acquisition of flexible planar source (red) wrapped around bare detector inside of R = 3.125 inch (inner radius) process component (blue).

The spectrum acquired in the configuration of Figure 5 is shown in Figure 6. The data acquired and the decay corrected efficiencies are listed in Table 1. From these data we implemented a log-log interpolation technique to determine an efficiency of 0.01127 for the 185.7-keV photon and of 0.00603 for the 414-keV photon. In this interpolation we exclude the Am-241 peak at 59 keV as it is beyond (lower in energy than) the peak of the efficiency curve for our detector. We disregard all detection rate uncertainties in the six peaks used and do not propagate error in our interpolations. These data yield a geometry factor of 0.01127/0.000905 = 12.45 for U-235 and of 0.00603/0.000474 = 12.72 for Pu-239 – very good agreement. Our mission is to approximately reproduce those ratios using cylindrical source flux calculations onto the detector faces and sides.

Table 1. Peak energies and detected areas for the cylindrical shell configuration.

Energy	Area	cps	branch	eff
58.89	117306(628)	587(3)	0.357	0.00283(1)
121.40	422838(1076)	2114(5)	0.284	0.01339(3)
244.48	83674(628)	418(3)	0.0751	0.01001(7)
344.07	227124(689)	1136(3)	0.266	0.00768(2)
661.25	287435(746)	1437(4)	0.8521	0.00434(1)
1111.08	42566(463)	213(2)	0.136	0.00283(3)
1211.77	3875(185)	19(1)	0.0140	0.0024(1)

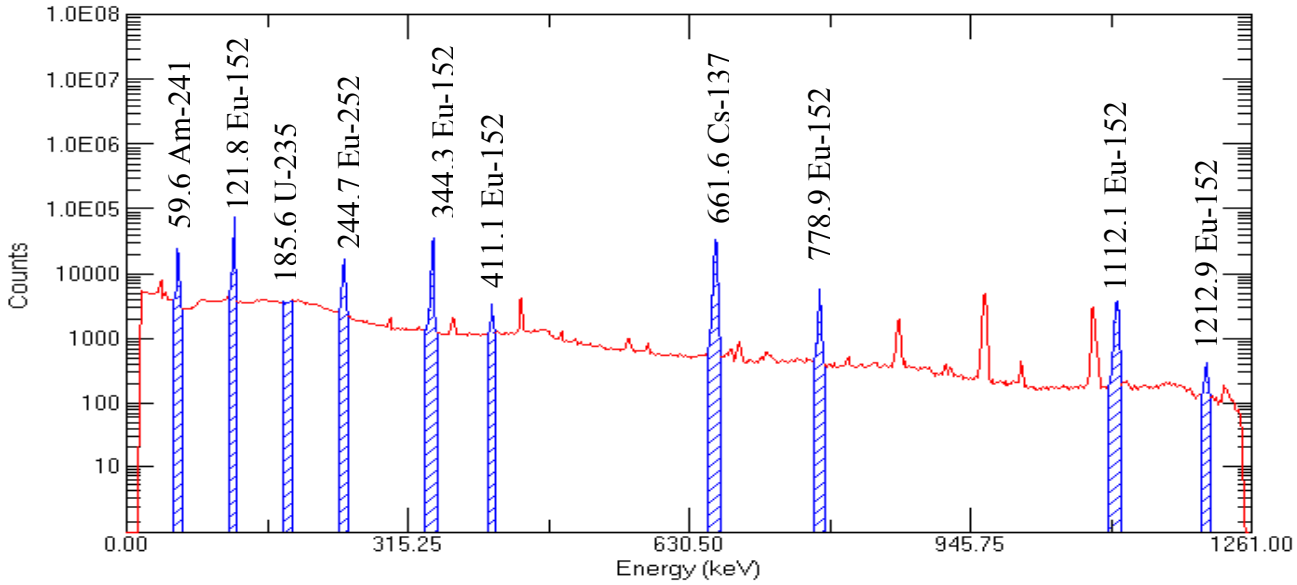

Figure 6. Cylindrical shell efficiency calibration spectrum of our HpGe detector.

In Figure 5 the dimensions h_1 and h_2 are $3_{15/16}$ inches and $4_{11/16}$ inches. Subtracting detector height and converting to centimeters, the distance h_2 to the rear face of the detector is 10.9165 cm. To determine the total flux of the source onto the front face of the detector we observe that (by exact analogy with Figure 1) for h_1, $\theta_1 = \text{Atan}(R/h_1) = \text{Atan}(3.125/3_{15/16}) = 38.437^\circ$, and $\theta_2 = 90^\circ$. For h_2, $\theta_1 = \text{Atan}(R/h_2) = \text{Atan}(0.72711) = 36.021^\circ$, and $\theta_2 = 90^\circ$. Solving (1) then yields a flux of $0.18917S_a$ reaching the front detector face, and a flux of $0.20596S_a$ reaching the back detector face.

How does this compare to the flux from comparable point source exposing the detector from a distance of 12 inches? The flexible source S_a is 1187.6 cm^2 in area, and so is equivalent to a point source spread over that surface area. $S_{pt} = S_a/1187.6$ dps/cm^2. At 12 inches the point source flux on the front detector is

$$\Phi(pt) = S_{pt}/\{4\pi(12x2.54)^2\} = 8.5656x10^{-5}S_{pt}. \qquad (5)$$

And so we seek a cylindrical source flux such that the ratio $\Phi(A)/\Phi(pt) = 12.6$ is maintained. That is, we seek a multiple *n* such that

$$(nS_a/1187.6)/0.000085656S_{pt} = 12.6. \qquad (6)$$

That sum must be approximately three times $n = (0.20596 + 0.18917)$ to satisfy (6).

Results

The results for the cylindrical shell original detector (m-det) acquisition at 20” yield the detection rates and decay corrected efficiencies listed in Table 2, and the acquisition at 13” with the second detector yield the efficiencies listed in Table 3. For this 2010 data,

the original detector and the second detector were recalibrated in the 12-inch point source configuration using a new Ho-166^m point source of 10.48 μCi.[14] The plots of the two efficiency curves are very similar in shape to that of Figure 3, but do not agree with it exactly. The best fit to the new calibration curve for the original detector (m-det) is

$$\ln(\text{eff}) = -8.373 + 0.9371x - 0.07763x^2 - 0.05631x^3 + 0.1294x^4 - 0.05321x^5, \quad (7)$$

where x = ln(947.8/E), and to the second detector (MRS-det) is

$$\ln(\text{eff}) = -7.651 + 0.7281x + 0.1104x^2 + 0.07461x^3 - 0.2435\,x^4, \quad (8)$$

where x = ln(445.4/E).

The last column in each of Tables 2 and 3 lists the decay-corrected detection efficiency relative to the 12-inch point source for each photon energy. This column in each table demonstrates the energy independence of the detection ratios in the cylindrical source to point source configurations.

In Table 2 we use the same log-log interpolation technique to obtain the detection efficencies of 0.000166 and 0.000112 for the 185.7- and 414-keV primary γ-rays from U-235 and Pu-239 for the 20" cylindrical acquisition. These two results yield geometry corrections compared to the 12-inch point source measurement of 0.2096 and 0.2258. But even without interpolation we observe geometry corrections for the 244-, 344-, and 661-keV photons of 0.2354, 0.2203, and 0.1986.

Using the 13" cylindrical acquisition we obtain the extremes of θ in equation (1) of θ_{min} = 7.86402° and θ_{max} = 13.5166°. That is θ_{max} = Atan(3.125/13) = Atan(0.24038) and θ_{min} = Atan(3.125/[13 +9.625]) = Atan(0.13812). Therefore the flux on the detector face is

$$\Phi_{13}(A) = -0.5[\sin(7.8640°) - \sin(13.517°)]S_{area} \quad (1)$$

$$= 0.048454S_{area}.$$

Since $S_{area} = S_a/1187.6$, we have

$$(0.048454S_a/1187.6)/0.000085656S_{pt} = 0.4763S(\text{12-inch point source}),$$

which should hold for all energies. For the 185.7-keV γ-ray from U-235 we should observe for example an efficiency in the 13-inch cylindrical field $\text{eff}_{cyl}(185.7)$ = 0.000905(0.4763) = 0.000431. In Table 3 we have an overall cylindrical to point source ratio of 0.4614(283) in excellent agreement with the calculated value of 0.4763.

For the 20-inch cylindrical field source we have

$$\Phi_{20}(A) = -0.5[\sin(6.0216) - \sin(8.8807)]S_{area} \quad (1)$$

$$= \quad 0.02474S_{area}$$

$$= \quad 0.2432S(\text{12-inch point source}),$$

and a geometry correction constant of 0.24320 relative to the 12-inch point source. The interpolated efficiency of the 185.7 γ-ray in the 20-inch cylindrical field should be 0.00022001. We note in Table 2 that interpolated value is approximately 0.00018. In Table 2 we observe an overall cylindrical to point source detection rate of 0.2133(136). Agreement is not quite as good as in Table 3. We do not tabulate the complete data for the 12", 23", and 29" acquisitions, but note the calculated geometry correction ratios are 0.5357, 0.1931, and 0.1302. The measured ratios are 0.4285(213), 0.1946(61), and 0.1101(85).

We observe much better agreement when using the second detector (mrs-det) and for the larger acquisition distances. But overall agreement between experiment and theory is favorable.

Table 2. Measured detection rates and efficiencies with the second detector (m-det) using a cylindrical acqusition configuration and a 20" standoff distance.

Eγ(keV)	branch	A(counts)	σ(A)	cps	eff	eff(12-inch)	Geo factor
59.2	0.357	11001	139	4.58375	0.0000225	0.000191	0.11775
121.7	0.284	41073	234	17.11375	0.0001868	0.000887	0.210591
244.4	0.0751	9552	130	3.98	0.0001643	0.000698	0.235355
343.8	0.266	25049	178	10.43708	0.0001216	0.000552	0.22034
443.5	0.028	2285	80	0.952083	0.0001054	0.000472	0.223311
661.3	0.8521	42379	226	17.65792	0.0000681	0.000343	0.198607
778.6	0.1298	5776	88	2.406667	0.0000575	0.000288	0.199565
867	0.0421	1701	56	0.70875	0.0000522	0.000254	0.205453
						Ave	0.213318
						St dev	0.013599

Table 3. Measured detection rates and efficiencies with the original detector (mrs-det) using a cylindrical acqusition configuration and a 13" standoff distance.

Eγ(keV)	branch	A(counts)	σ(A)	cps	eff	eff(12-inch)	Geo factor
59.4	0.357	18917	182	18.917	0.0000928	0.000191	0.485949
121.7	0.284	36297	236	36.297	0.0003962	0.000881	0.449689
244.6	0.0751	8187	133	8.187	0.0003379	0.000707	0.47797
344.1	0.266	21989	176	21.989	0.0002562	0.000552	0.464216
367.9	0.00858	746	78	0.746	0.0002695	0.000525	0.513367
410.6	0.0223	1464	90	1.464	0.0002035	0.000483	0.421332
443.8	0.028	2010	80	2.01	0.0002225	0.000456	0.487988
661.7	0.8521	40258	213	40.258	0.0001553	0.000337	0.460864
779.1	0.1298	5401	85	5.401	0.0001290	0.000297	0.434289
867.6	0.0421	1661	59	1.661	0.0001223	0.000273	0.447982
964.4	0.145	5030	80	5.03	0.0001075	0.000251	0.428412
						Ave	0.461096
						St dev	0.028351

A good analysis to determine agreement with equation (1) for both detectors requires a thorough analysis of our uncertainty in these cylindrical shell acquisitions. Reference 2 states an uncertainty of approximately 3% in each of the 12-inch point source efficiencies, and reference 10 demonstrates a slightly larger uncertainty for detector two. We estimate an uncertainty in our acquisition distances of another 6%. This uncertainty includes detector recess inside the detector housing.

Looking at the photograph of Figure 4, the reader can see that the flexible planar source did not form a perfectly circular cylinder with uniformly smooth sides. We used line of sight to place the cylindrical axis of the source to coincide exactly with the cylindrical axis of the detector. A 1% uncertainty there yields an uncertainty of approximately 2% in $R\csc\theta$, which is the important component of r in equation (1). The cylinder axis was set up and assumed to have radius R = 3.125 inches in (1). We assume an uncertainty of 4% (i.e. ± 0.125 inches). The reader can confirm that yields an uncertainty of approximately 5% in the difference $[\sin(\theta_2) - \sin(\theta_1)]$ in (1).

Finally we estimate the uncertainty in r including a finite detector face in Figure 1. The largest possible uncertainty would be in the 12-inch cylindrical acquisition where we calculate $R\csc\theta$ for both the center of the detector face and for an extreme outer portion of the detector r_o. This extreme difference would increase r by 2.5%, for a 5% reduction in point detection efficiency. While 5% is the extreme, we note a photon striking the detector face at the extreme r_o will also have an increased Compton component compared to one striking the center of the detector face. These two effects do not only introduce an uncertainty, but they introduce a *reduction* in detection efficiency. Conservatively we include only another 1% contribution to the uncertainty of the detection efficiency from this component. But we note this uncertainty without doubt introduces a negative bias (that we have tended to observe) in the measured detection efficiency.

The vendor does not include a stated uncertainty in the planar source certificate nor in the stated uncertainty in the uniformity of the planar activity, but a scan of a similar planar source made by the same vendor indicates the uniformity could vary by as much as 7%.[13] We have arbitrarily included another 3% in the total source uncertainty. We include no statistical uncertainty in any of our acquisitions. Our quadratic sum of uncertainty of detection efficiency for the five (12-, 13-, 20-, 23-, and 29-inch) cylindrical source acquisitions is (9 – 11)% one-sigma.

Reconciliation of measured geometry correction for bare detector cylindrical source

We now return to equation (6) to attempt to explain theoretically how we can observe a measured geometry factor of 12.6 when exposing the bare detector to the finite cylindrical source shown in Figure 5. Clearly the fraction of flux that reaches the two faces is not adequate. We have to include the flux reaching the sides of the cylindrical detector itself. We model that separately in Figures 7 and 8.

In Figure 7 we show the portion of the cylindrical source that is directly opposite the cylindrical sides of the detector and is irradiating face to face at a right angle to the

detector sides. We refer to this perpendicular flux onto the sides of the detector as $\Phi_{\perp}(A)$. That small portion of the source that is 3.53 cm long and does not overlap the ends of the detector does not radiate onto either face, but radiates with no loss of flux in the inward direction on to the exposed side. This is in exact analogy to a finite area source configuration irradiating perpendicularly onto the front face of the detector.

We model this 3.53-cm portion of the source as consisting of a parallel beam of flux irradiating onto the detector and a parallel beam of flux irradiating away from the detector. That is, 50% of the beam in the fraction of the source 3.53/(9.625x2.54) is striking the detector. This adds

$$\Phi_{\perp}(A) = 0.5(3.53)S_a/(9.625x2.54) = 0.072196S_a, \quad (9)$$

to *n,* and is only a tiny fraction of the flux we seek to reconcile (6).

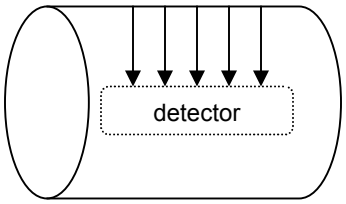

Figure 7. Model of a parallel beam of photons irradiating inwardly from the source to the detector's cylindrical side.

We next seek to model that portion of the cylindrical source that extends out from the detector front face to h_1 and is irradiating onto the cylindrical sides as shown in Figure 8.

$$r = \rho\csc\theta$$
$$h = \rho\cot\theta$$

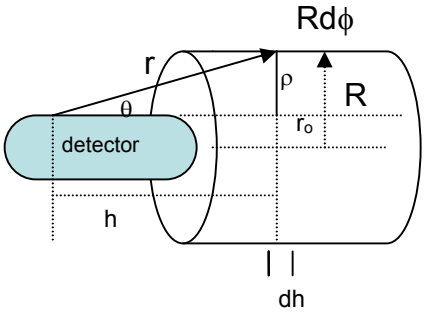

$$dA = dhR\sin\theta d\phi$$
$$\rho = R - r_o$$
$$dh = -\rho\csc^2\theta d\theta$$

Figure 8. Schematic illustration of determination of flux irradiating on to the sides of the detector.

While the illustration of Figure 7 allows an exact solution of the flux leaving the cylindrical source striking an arbitrary point [$\Phi_s(A)$] on the detector side, it does not lend itself to a closed solution for summing over the whole cylindrical side of the detector $\Phi_{\Sigma s}(A)$. In our model, we use exact calculus to integrate over the source area to determine the flux $\Phi_s(A)$ striking a designated detector slice ds, but we use a sum over slices ds to calculate the total flux reaching the whole detector side.

From Figure 8 we note the differential flux reaching the slice of detector ds is

$$d\Phi_s(A) = S_a dA/4\pi r^2, \qquad (10)$$

where A and dA refer to the area of the cylindrical source. Therefore the total flux integrated over the entire source area irradiating onto the slice ds is

$$\Phi_s(A) = S_a/4\pi\{\int_h\int_\phi dA/r^2\} = (S_a/4\pi)\int_h\int_\phi dhR\sin\theta d\phi/r^2 \qquad (11)$$
$$= (S_a/4\pi)\{\int_\theta\int_\phi -\rho\csc^2\theta R\sin\theta d\theta d\phi/\rho^2\csc^2\theta\},$$

which reduces to

$$\Phi_s(A) = -(S_a/4\pi)\{\int_h\int_\phi R\sin\theta d\theta d\phi/\rho\}. \quad (12)$$

Integrating over θ

$$\Phi_s(A) = (S_a/4\pi)\{\int_\phi R\cos\theta d\phi/\rho\}, \quad (13)$$

and over ϕ

$$\Phi_s(A) = RS_a\cos\theta/2\rho, \quad (14)$$

where θ is evaluated at the limits of the end of the source and where the source becomes tangent to the detector face.

An exact solution of the flux reaching the detector side would involve writing h and r as a function of s, then simultaneously solving for $\Phi_s(A)/\int ds$. This becomes very complex. Instead we choose to hold s constant to obtain the integral $\Phi_s(A)$ for a series of ds slices and then to average over those ds's to yield an approximate value for the sum $\Phi_{\Sigma s}(A)$.

To proceed we use a single example slice of the detector ds and a single example slice of the portion of the source that extends from the front face of the detector to h_1 in Figures 5 and 8. We show example calculations in the Excel spreadsheet of Table 4. In Table 4 we have divided the portion of the source from h_0 to h_1 into eleven slices dh equal to 0.909205 cm ($3^{15/16}$ in x 2.54/11). We have divided the detector into eight slices ds equal to 0.441325 cm. We then perform the sum over i (dh) for each segment j (ds) to calculate each $d\Phi_{ij}$ to get Φ_s. We also perform the exact calculus solution of equation (14) to determine Φ_s. We then sum the sums over s and separately sum the exact calculus solutions over s to obtain two values of $\Phi_{\Sigma s}(A)$ for evaluation.

For our example calculation we take the j = 5 segment of the detector and the h_1 side of the source. This 5th segment approximately equals the segment we depict in Figure 8. We sum and integrate separately over the line that forms equivalently the top of the source and then sum and integrate separately around the circumference (ϕ) of the source. In our example h runs from the midpoint of ds (j=5) to h_{max} at the h_1 end of the source and to h_{min} at the end of the detector. The reader can determine that

$$h_{max} = 4ds + 0.5ds + h_1 - 0.5dh = 1.76530 + 0.22066 + 10.00125 - 0.45460 \quad (15)$$

$$= 11.53265.$$

In our sum h then increments down by dh to

$$h_{min} = 4ds + 0.5ds + 0.5dh = 2.44056. \quad (16)$$

In the spreadsheet of Table 4 we calculate (for i=1,j=5) r^2, θ(in radians), sinθ, and flux(ij). For all i and j on either source end $\rho = R - r_o = 5.19430$ cm. $r_{(15)}^2 = h^2 + \rho^2 = 159.9818$. $\theta = \text{Atan}(r/h) = \text{Atan}(5.1943/11.53265) = 0.4232$rad, $\sin\theta = 0.41067$, and flux(ij) is

$$d\Phi_s(A) = S_a dA/4\pi r^2, \quad (17)$$

$$= S_a(dh)(\sin\theta)R/4\pi r^2.$$

In column ten we tabulate $(dh)(\sin\theta)/4\pi r^2$. For i,j = 1,5 that is 0.00018573. We then obtain the sum over i of all j segments of $(dh)(\sin\theta)/4\pi r^2$. That sum appears in column eleven. For the j=5 segment of the detector we have "Sum $h_{15} = 0.0085713$".

In Table 4 we then sum column eleven to obtain the sum over j for h_1, "Sum of all rings $h_{1j} = 0.074128244$. This sum is equivalent to $\Sigma_i(dh)\sin\theta/4\pi r^2$, and so to obtain $\Phi_{\Sigma s}(A)$ we multiply by $\int R d\phi = 2\pi R$. That element appears immediately below the sum over i, and is equal to 3.696981854. We then divide by $\int ds$, or equivalently by 8, the number of j segments. Finally our sum for h_1 is $\Phi_{\Sigma s}(A) = 0.4621 S_a$, shown at the bottom of column twelve.

We now return to the exact calculus solution for $\Phi_s(A)$ and compare. We again use the example of the j=5 segment of the detector and apply equation (14). For this segment ds we have already noted the extremes of θ are determined by $\text{Atan}(h_{max}/\rho) = 0.4232$rad and $\theta_{min} = 1.1316$ rad. Upon evaluation of the integral in (14) we obtain

$$\Phi_s(A) = RS_a/2\rho[\cos(0.4232) - \cos(1.1316)] = 0.2432RS_a/\rho) \quad (18)$$

$$= 0.3717S_a,$$

and this value is tabulated in column twelve at the top of the j=5 segment of Table 4.

We evaluate the integral $\Phi_s(A)$ for each segment j and tabulate at the top of column twelve in each segment of the Table. At the bottom of column thirteen we sum column twelve (sum of calculus = 3.2364) and average (divide by the 8, j segments) to obtain $\Phi_{\Sigma s}(A) = 0.4045 S_a$ in column fourteen.

In the **Discussion** section we defend the results of the various sum of sums and sum of exact calculus by several comparisons and several tabulations. We also defend dividing the detector into only 8 segments instead of proceeding to smaller segments ds and smaller segments dh. For now we accept the results of Table 4 and of the similar calculations performed in Table 5 for the section h_2 of the source. We leave it to the reader to duplicate the remaining calculations in Table 4 and to duplicate those of Table 5. In the latter we divided the source into twelve sections dh = 0.9096 cm, and we again

select ds = 2.2066 cm for the detector. In Table 5 we obtain $\Phi_{\Sigma s}(A) = 0.470398S_a$ for the sum of sums result and $\Phi_{\Sigma s}(A) = 0.340083S_a$ for the sum of calculus results. In both tables we accept the sum of calculus results and evaluate equation (6) to sum the entire area source flux striking both ends and the sides of the detector.

We now have results for the flux striking both detector faces ($0.18917S_a$ and $0.20596S_a$), for the perpendicular flux striking the detector sides ($0.072208S_a$), and for the oblique flux striking the detector sides ($0.4045S_a$ and $0.340083S_a$). In (6) we then have

$$n = 0.18917 + 0.20596 + 0.072208 + 0.4045 + 0.340083) = 1.2119, \qquad (19)$$

in very good agreement with the required value of $n = 1.2817$ that we seek to make (6) equal to 12.6.

Discussion

We note several phenomena in Tables 4, 5, and 6 that we discuss in this section. In Table 6 we list several results where we have divided the detector and h_1 side of the source into only one, two, three, or four segments. We have highlighted in bold the sum of sums results and the sum of calculus results. We note that as we increase the number of segments, (that is the slices ds and dh get smaller) the two values approach each other and approach the values obtained for eleven sources slices and eight detector slices. This is completely expected, but still lends credibility to the two techniques of calculation.

We note further that the ratio between the sum and the exact calculus for each individual ring remains constant as we increment j. That is the ratio "sum of ring" to $R\cos\theta/2\rho$ is constant for each increment j in all segments i. The sum of ring value is equal to $\Sigma_i dh\sin\theta/4\pi r^2$, holding j constant, or $\Phi_s(A)/\int Rd\phi$. Therefore that value divided by the individual exact calculus value for the segment j should be a constant from segment to segment.

For example, the exact calculus for ring j = 1 in Table 4 is 0.5761, and the sum for that ring is 0.013007 for a ratio of 0.02258. Moving to ring j = 2, the ratio is 0.011831/0.5204 = 0.02273. Progressing down the h_1 source side for all detector segments j, the ratio yields an average value of 0.02295(21), where 21 is the standard deviation σ in the last two digits. That σ_{rel} is 0.92%. We note that both the sum and calculus decrease as we increment j because $\sin\theta$ and r are varying appropriately to yield the results. We note the same phenomenon with the h_2 side of the source in Table 5. Including that side in the average and standard deviation yields 0.02290(21).

The ratio is very strongly dependent upon the number of segments ds we choose, but it still remains constant for each segment j within our choice, as we can demonstrate in Table 6. Note the composite ratio for the two source segments, two detector segments portion of Table 6 is 2.3323(122). For the three source segments, three detector segments portion the ratio is 1.7022(255), and for the four source segments, four detector segments portion it is 1.4703(235). We believe this constant ratio as we increment j also lends

substantial credibility to the technique of determining flux impinging on the cylindrical sides of the detector from the cylindrical source.

Conclusion

In this paper we have used two detectors and three distinct detector calibrations to demonstrate the use of exact calculus to determine the geometry correction factor that relates the cylindrical source acquisition configuration to a point source configuration. Our data and analysis confirms the derivations of reference 1.

We have also derived a method to satisfactorily model the 4π flux impinging on the detector faces and detector sides for the bare (nshielded and un-collimated) detector cylindrical source acquisition configuration. This bare detector acquisition configuration was implemented as the oven source configuration for modeling U-235 holdup content in process components of the Savannah River Site Uranium Fuel Fabrication Facility and is described in the invention disclosure of reference 3.

The modeling of the bare source does not lend itself to a closed calculus exact solution. The sums for the cylindrical sides of the source and detector are modeled using a combination of exact calculus for the source are and finite sums for the detector area. In our **Results** section we demonstrate adequate convergence using eight detector segments and up to twelve source segments to yield calculated detection efficiency in excellent agreement with measured detection efficiency. In the **Discussion** section we use descriptive quantitative comparisons to lend credibility to the evaluation.

Table 4. Determination of flux on Cylindrical Detector Side from h_1 source side. $\phi = S/4\pi r^2$ line source

i	j	h_{1i}	ρ_{1j}	$r_{ij\ squared}$	θ(rad)	sin(θ)	d(s)	dh	flux(S)		
1	1	9.7673	5.1943	122.3811	0.4888	0.4695	2.2066	0.9092	2.7759E-04		0.5761
2	1	8.8581	5.1943	105.4468	0.5304	0.5058	2.2066	0.9092	3.4708E-04		
3	1	7.9489	5.1943	90.16576	0.5788	0.5470	2.2066	0.9092	4.3895E-04		
4	1	7.0397	5.1943	76.53806	0.6357	0.5937	2.2066	0.9092	5.6126E-04		
5	1	6.1305	5.1943	64.56366	0.7029	0.6464	2.2066	0.9092	7.2443E-04		
6	1	5.2213	5.1943	54.24257	0.7828	0.7053	2.2066	0.9092	9.4074E-04		
7	1	4.3121	5.1943	45.57479	0.8779	0.7694	2.2066	0.9092	1.2215E-03		
8	1	3.4029	5.1943	38.56031	0.9908	0.8365	2.2066	0.9092	1.5695E-03		
9	1	2.4937	5.1943	33.19914	1.1232	0.9015	2.2066	0.9092	1.9647E-03		
10	1	1.5845	5.1943	29.49128	1.2747	0.9565	2.2066	0.9092	2.3466E-03		
11	1	0.6753	5.1943	27.43673	1.4415	0.9917	2.2066	0.9092	2.6151E-03		
									Sum ring h_{1j}	1.3007E-02	
1	2	10.2086	5.1943	131.197	0.4707	0.4535	2.2066	0.9092	2.5009E-04		0.5204
2	2	9.2994	5.1943	113.4602	0.5094	0.4876	2.2066	0.9092	3.1097E-04		
3	2	8.3902	5.1943	97.37663	0.5543	0.5264	2.2066	0.9092	3.9111E-04		
4	2	7.4810	5.1943	82.94641	0.6069	0.5703	2.2066	0.9092	4.9749E-04		
5	2	6.5718	5.1943	70.1695	0.6689	0.6201	2.2066	0.9092	6.3938E-04		
6	2	5.6626	5.1943	59.0459	0.7423	0.6760	2.2066	0.9092	8.2831E-04		
7	2	4.7534	5.1943	49.57561	0.8297	0.7377	2.2066	0.9092	1.0767E-03		
8	2	3.8442	5.1943	41.75863	0.9337	0.8038	2.2066	0.9092	1.3927E-03		
9	2	2.9350	5.1943	35.59495	1.0565	0.8706	2.2066	0.9092	1.7697E-03		
10	2	2.0258	5.1943	31.08458	1.1989	0.9317	2.2066	0.9092	2.1685E-03		
11	2	1.1166	5.1943	28.22751	1.3591	0.9777	2.2066	0.9092	2.5059E-03		
									Sum ring h_{1j}	1.1831E-02	

Table 4 (Continued).

1	3	10.6500	5.1943	140.4024	0.4538	0.4384	2.2066	0.9092	2.2590E-04		0.4672
2	3	9.7408	5.1943	121.8631	0.4899	0.4705	2.2066	0.9092	2.7936E-04		
3	3	8.8316	5.1943	104.977	0.5317	0.5070	2.2066	0.9092	3.4941E-04		
4	3	7.9223	5.1943	89.7443	0.5803	0.5483	2.2066	0.9092	4.4205E-04		
5	3	7.0131	5.1943	76.16489	0.6375	0.5952	2.2066	0.9092	5.6539E-04		
6	3	6.1039	5.1943	64.23877	0.7051	0.6481	2.2066	0.9092	7.2993E-04		
7	3	5.1947	5.1943	53.96597	0.7854	0.7071	2.2066	0.9092	9.4798E-04		
8	3	4.2855	5.1943	45.34648	0.8810	0.7714	2.2066	0.9092	1.2307E-03		
9	3	3.3763	5.1943	38.38029	0.9944	0.8384	2.2066	0.9092	1.5806E-03		
10	3	2.4671	5.1943	33.06741	1.1274	0.9033	2.2066	0.9092	1.9764E-03		
11	3	1.5579	5.1943	29.40784	1.2794	0.9578	2.2066	0.9092	2.3566E-03		
									Sum ring h_{1j}	1.0684E-02	
1	4	11.0913	5.1943	149.9974	0.4380	0.4241	2.2066	0.9092	2.0458E-04		0.4175
2	4	10.1821	5.1943	130.6555	0.4717	0.4544	2.2066	0.9092	2.5164E-04		
3	4	9.2729	5.1943	112.967	0.5106	0.4887	2.2066	0.9092	3.1301E-04		
4	4	8.3637	5.1943	96.93173	0.5558	0.5276	2.2066	0.9092	3.9380E-04		
5	4	7.4545	5.1943	82.5498	0.6086	0.5717	2.2066	0.9092	5.0108E-04		
6	4	6.5453	5.1943	69.82118	0.6708	0.6216	2.2066	0.9092	6.4417E-04		
7	4	5.6361	5.1943	58.74587	0.7446	0.6777	2.2066	0.9092	8.3467E-04		
8	4	4.7269	5.1943	49.32386	0.8325	0.7396	2.2066	0.9092	1.0849E-03		
9	4	3.8176	5.1943	41.55517	0.9370	0.8058	2.2066	0.9092	1.4029E-03		
10	4	2.9084	5.1943	35.43978	1.0604	0.8725	2.2066	0.9092	1.7813E-03		
11	4	1.9992	5.1943	30.97769	1.2034	0.9333	2.2066	0.9092	2.1797E-03		
									Sum ring h_{1j}	9.5919E-03	

Table 4 (Continued).

1	5	11.5326	5.1943	159.9818	0.4232	0.4107	2.2066	0.9092	1.8573E-04	0.3717
2	5	10.6234	5.1943	139.8375	0.4548	0.4393	2.2066	0.9092	2.2727E-04	
3	5	9.7142	5.1943	121.3464	0.4910	0.4715	2.2066	0.9092	2.8115E-04	
4	5	8.8050	5.1943	104.5087	0.5330	0.5081	2.2066	0.9092	3.5176E-04	
5	5	7.8958	5.1943	89.32425	0.5819	0.5496	2.2066	0.9092	4.4517E-04	
6	5	6.9866	5.1943	75.79312	0.6393	0.5966	2.2066	0.9092	5.6955E-04	
7	5	6.0774	5.1943	63.9153	0.7072	0.6497	2.2066	0.9092	7.3548E-04	
8	5	5.1682	5.1943	53.69079	0.7879	0.7089	2.2066	0.9092	9.5528E-04	
9	5	4.2590	5.1943	45.11958	0.8840	0.7733	2.2066	0.9092	1.2400E-03	
10	5	3.3498	5.1943	38.20168	0.9980	0.8404	2.2066	0.9092	1.5917E-03	
11	5	2.4406	5.1943	32.93709	1.1316	0.9051	2.2066	0.9092	1.9882E-03	
									Sum ring h_{1j}	8.5713E-03
1	6	11.9739	5.1943	170.3559	0.4093	0.3980	2.2066	0.9092	1.6902E-04	0.3303
2	6	11.0647	5.1943	149.409	0.4389	0.4250	2.2066	0.9092	2.0579E-04	
3	6	10.1555	5.1943	130.1154	0.4728	0.4554	2.2066	0.9092	2.5321E-04	
4	6	9.2463	5.1943	112.4752	0.5118	0.4898	2.2066	0.9092	3.1506E-04	
5	6	8.3371	5.1943	96.48824	0.5572	0.5288	2.2066	0.9092	3.9652E-04	
6	6	7.4279	5.1943	82.1546	0.6103	0.5731	2.2066	0.9092	5.0470E-04	
7	6	6.5187	5.1943	69.47427	0.6728	0.6232	2.2066	0.9092	6.4900E-04	
8	6	5.6095	5.1943	58.44724	0.7470	0.6794	2.2066	0.9092	8.4107E-04	
9	6	4.7003	5.1943	49.07353	0.8353	0.7415	2.2066	0.9092	1.0932E-03	
10	6	3.7911	5.1943	41.35312	0.9403	0.8077	2.2066	0.9092	1.4132E-03	
11	6	2.8819	5.1943	35.28601	1.0643	0.8744	2.2066	0.9092	1.7930E-03	
									Sum ring h_{1j}	7.6338E-03

Table 4 (Continued).

1	7	12.4153	5.1943	181.1194	0.3963	0.3860	2.2066	0.9092	1.5418E-04			0.2931	
2	7	11.5061	5.1943	159.3701	0.4241	0.4115	2.2066	0.9092	1.8680E-04				
3	7	10.5969	5.1943	139.274	0.4558	0.4401	2.2066	0.9092	2.2865E-04				
4	7	9.6876	5.1943	120.8312	0.4922	0.4725	2.2066	0.9092	2.8295E-04				
5	7	8.7784	5.1943	104.0418	0.5343	0.5092	2.2066	0.9092	3.5413E-04				
6	7	7.8692	5.1943	88.90561	0.5834	0.5509	2.2066	0.9092	4.4832E-04				
7	7	6.9600	5.1943	75.42277	0.6411	0.5981	2.2066	0.9092	5.7375E-04				
8	7	6.0508	5.1943	63.59324	0.7094	0.6514	2.2066	0.9092	7.4108E-04				
9	7	5.1416	5.1943	53.41701	0.7905	0.7107	2.2066	0.9092	9.6263E-04				
10	7	4.2324	5.1943	44.89409	0.8871	0.7752	2.2066	0.9092	1.2494E-03				
11	7	3.3232	5.1943	38.02448	1.0016	0.8424	2.2066	0.9092	1.6028E-03				
									Sum ring h_{1j}	6.7847E-03			
1	8	12.8566	5.1943	192.2725	0.3840	0.3746	2.2066	0.9092	1.4096E-04			0.2601	
2	8	11.9474	5.1943	169.7206	0.4101	0.3987	2.2066	0.9092	1.6997E-04		Sum of all calculus		3.2364	**0.4045**
3	8	11.0382	5.1943	148.8221	0.4398	0.4258	2.2066	0.9092	2.0700E-04				
4	8	10.1290	5.1943	129.5768	0.4738	0.4563	2.2066	0.9092	2.5479E-04				
5	8	9.2198	5.1943	111.9848	0.5131	0.4908	2.2066	0.9092	3.1713E-04				
6	8	8.3106	5.1943	96.04616	0.5586	0.5300	2.2066	0.9092	3.9926E-04				
7	8	7.4014	5.1943	81.76081	0.6119	0.5745	2.2066	0.9092	5.0835E-04				
8	8	6.4922	5.1943	69.12876	0.6748	0.6247	2.2066	0.9092	6.5387E-04				
9	8	5.5829	5.1943	58.15003	0.7494	0.6812	2.2066	0.9092	8.4753E-04				
10	8	4.6737	5.1943	48.8246	0.8381	0.7434	2.2066	0.9092	1.1016E-03				
11	8	3.7645	5.1943	41.15248	0.9437	0.8097	2.2066	0.9092	1.4236E-03				
									Sum ring h_{1j}	6.0241E-03			
									Sum all rings h_{1j}	0.074128244			
									Sum times Rdϕ	3.696981854	**0.4621**		

Table 5. Determination of flux on Cylinder Dectector Side from h2 source side. $\phi = S/4\pi r^2$ line source

i	j	h_{2i}	ρ_{2j}	$r_{ij\ squared}$	θ(rad)	sin(θ)	d(s)	dh	flux(S)		
1	1	10.6815	5.1943	141.0751	0.4526	0.4373	2.2066	0.9096	0.000224		0.588591
2	1	9.7719	5.1943	122.4699	0.4886	0.4694	2.2066	0.9096	0.000277		
3	1	8.8622	5.1943	105.5197	0.5301	0.5057	2.2066	0.9096	0.000347		
4	1	7.9526	5.1943	90.2243	0.5786	0.5468	2.2066	0.9096	0.000439		
5	1	7.0429	5.1943	76.58381	0.6355	0.5936	2.2066	0.9096	0.000561		
6	1	6.1333	5.1943	64.5982	0.7027	0.6463	2.2066	0.9096	0.000724		
7	1	5.2237	5.1943	54.26747	0.7826	0.7051	2.2066	0.9096	0.000941		
8	1	4.3140	5.1943	45.59162	0.8777	0.7693	2.2066	0.9096	0.001221		
9	1	3.4044	5.1943	38.57065	0.9906	0.8364	2.2066	0.9096	0.00157		
10	1	2.4948	5.1943	33.20456	1.1230	0.9014	2.2066	0.9096	0.001965		
11	1	1.5851	5.1943	29.49335	1.2746	0.9565	2.2066	0.9096	0.002347		
12	1	0.6755	5.1943	27.43703	1.4415	0.9917	2.2066	0.9096	0.002616		
									Sum ring $h2_j$	1.3233E-02	
1	2	11.1228	5.1943	150.6978	0.4369	0.4231	2.2066	0.9096	0.000203		0.531683
2	2	10.2132	5.1943	131.2898	0.4705	0.4533	2.2066	0.9096	0.00025		
3	2	9.3035	5.1943	113.5367	0.5092	0.4875	2.2066	0.9096	0.000311		
4	2	8.3939	5.1943	97.43841	0.5541	0.5262	2.2066	0.9096	0.000391		
5	2	7.4843	5.1943	82.99503	0.6067	0.5702	2.2066	0.9096	0.000497		
6	2	6.5746	5.1943	70.20653	0.6686	0.6199	2.2066	0.9096	0.000639		
7	2	5.6650	5.1943	59.07291	0.7421	0.6758	2.2066	0.9096	0.000828		
8	2	4.7554	5.1943	49.59417	0.8295	0.7376	2.2066	0.9096	0.001077		
9	2	3.8457	5.1943	41.77031	0.9335	0.8037	2.2066	0.9096	0.001393		
10	2	2.9361	5.1943	35.60133	1.0563	0.8706	2.2066	0.9096	0.00177		
11	2	2.0264	5.1943	31.08723	1.1988	0.9316	2.2066	0.9096	0.002169		
12	2	1.1168	5.1943	28.22801	1.3590	0.9777	2.2066	0.9096	0.002507		
									Sum ring $h2_j$	1.2035E-02	

Table 5 (Continued).

1	3	11.5641	5.1943	160.7102	0.4222	0.4097	2.2066	0.9096	0.000185	0.477447
2	3	10.6545	5.1943	140.4993	0.4536	0.4382	2.2066	0.9096	0.000226	
3	3	9.7449	5.1943	121.9432	0.4897	0.4704	2.2066	0.9096	0.000279	
4	3	8.8352	5.1943	105.0421	0.5315	0.5068	2.2066	0.9096	0.000349	
5	3	7.9256	5.1943	89.79579	0.5802	0.5481	2.2066	0.9096	0.000442	
6	3	7.0160	5.1943	76.20439	0.6373	0.5950	2.2066	0.9096	0.000565	
7	3	6.1063	5.1943	64.26788	0.7049	0.6479	2.2066	0.9096	0.00073	
8	3	5.1967	5.1943	53.98625	0.7852	0.7069	2.2066	0.9096	0.000948	
9	3	4.2870	5.1943	45.3595	0.8808	0.7712	2.2066	0.9096	0.001231	
10	3	3.3774	5.1943	38.38763	0.9943	0.8384	2.2066	0.9096	0.001581	
11	3	2.4678	5.1943	33.07064	1.1273	0.9032	2.2066	0.9096	0.001977	
12	3	1.5581	5.1943	29.40853	1.2794	0.9578	2.2066	0.9096	0.002358	
									Sum ring $h2_j$	1.0870E-02
1	4	12.0055	5.1943	171.112	0.4083	0.3971	2.2066	0.9096	0.000168	0.42676
2	4	11.0958	5.1943	150.0982	0.4378	0.4240	2.2066	0.9096	0.000204	
3	4	10.1862	5.1943	130.7393	0.4716	0.4543	2.2066	0.9096	0.000252	
4	4	9.2766	5.1943	113.0352	0.5104	0.4886	2.2066	0.9096	0.000313	
5	4	8.3669	5.1943	96.98608	0.5556	0.5274	2.2066	0.9096	0.000394	
6	4	7.4573	5.1943	82.5918	0.6084	0.5716	2.2066	0.9096	0.000501	
7	4	6.5476	5.1943	69.85239	0.6706	0.6215	2.2066	0.9096	0.000644	
8	4	5.6380	5.1943	58.76787	0.7445	0.6776	2.2066	0.9096	0.000835	
9	4	4.7284	5.1943	49.33822	0.8323	0.7395	2.2066	0.9096	0.001085	
10	4	3.8187	5.1943	41.56346	0.9368	0.8057	2.2066	0.9096	0.001403	
11	4	2.9091	5.1943	35.44358	1.0603	0.8725	2.2066	0.9096	0.001782	
12	4	1.9995	5.1943	30.97858	1.2033	0.9332	2.2066	0.9096	0.002181	
									Sum ring $h2_j$	9.7608E-03

Table 5 (Continued).

1	5	12.4468	5.1943	181.9034	0.3953	0.3851	2.2066	0.9096	0.000153		0.380179
2	5	11.5372	5.1943	160.0867	0.4230	0.4105	2.2066	0.9096	0.000186		
3	5	10.6275	5.1943	139.9249	0.4546	0.4391	2.2066	0.9096	0.000227		
4	5	9.7179	5.1943	121.418	0.4909	0.4714	2.2066	0.9096	0.000281		
5	5	8.8082	5.1943	104.5659	0.5328	0.5080	2.2066	0.9096	0.000352		
6	5	7.8986	5.1943	89.36873	0.5817	0.5495	2.2066	0.9096	0.000445		
7	5	6.9890	5.1943	75.82644	0.6391	0.5965	2.2066	0.9096	0.000569		
8	5	6.0793	5.1943	63.93902	0.7071	0.6496	2.2066	0.9096	0.000735		
9	5	5.1697	5.1943	53.70649	0.7878	0.7088	2.2066	0.9096	0.000955		
10	5	4.2601	5.1943	45.12883	0.8839	0.7732	2.2066	0.9096	0.00124		
11	5	3.3504	5.1943	38.20606	0.9979	0.8404	2.2066	0.9096	0.001592		
12	5	2.4408	5.1943	32.93817	1.1315	0.9051	2.2066	0.9096	0.001989		
									Sum ring h2j	8.7254E-03	
1	6	12.8881	5.1943	193.0844	0.3831	0.3738	2.2066	0.9096	0.00014		0.337964
2	6	11.9785	5.1943	170.4648	0.4092	0.3978	2.2066	0.9096	0.000169		
3	6	11.0688	5.1943	149.5001	0.4388	0.4248	2.2066	0.9096	0.000206		
4	6	10.1592	5.1943	130.1902	0.4726	0.4552	2.2066	0.9096	0.000253		
5	6	9.2496	5.1943	112.5353	0.5117	0.4896	2.2066	0.9096	0.000315		
6	6	8.3399	5.1943	96.53521	0.5570	0.5287	2.2066	0.9096	0.000396		
7	6	7.4303	5.1943	82.19002	0.6101	0.5730	2.2066	0.9096	0.000505		
8	6	6.5207	5.1943	69.49971	0.6727	0.6231	2.2066	0.9096	0.000649		
9	6	5.6110	5.1943	58.46428	0.7469	0.6793	2.2066	0.9096	0.000841		
10	6	4.7014	5.1943	49.08374	0.8352	0.7414	2.2066	0.9096	0.001093		
11	6	3.7917	5.1943	41.35807	0.9402	0.8077	2.2066	0.9096	0.001414		
12	6	2.8821	5.1943	35.28729	1.0642	0.8744	2.2066	0.9096	0.001794		
									Sum ring $h2_j$	7.7747E-03	

Table 5 (Continued).

1	7	13.3294	5.1943	204.6548	0.3716	0.3631	2.2066	0.9096	0.000128		0.300127		
2	7	12.4198	5.1943	181.2323	0.3961	0.3858	2.2066	0.9096	0.000154				
3	7	11.5102	5.1943	159.4647	0.4239	0.4113	2.2066	0.9096	0.000187				
4	7	10.6005	5.1943	139.352	0.4556	0.4400	2.2066	0.9096	0.000229				
5	7	9.6909	5.1943	120.8942	0.4920	0.4724	2.2066	0.9096	0.000283				
6	7	8.7813	5.1943	104.0912	0.5342	0.5091	2.2066	0.9096	0.000354				
7	7	7.8716	5.1943	88.94313	0.5833	0.5508	2.2066	0.9096	0.000448				
8	7	6.9620	5.1943	75.44994	0.6410	0.5980	2.2066	0.9096	0.000574				
9	7	6.0523	5.1943	63.61162	0.7093	0.6513	2.2066	0.9096	0.000741				
10	7	5.1427	5.1943	53.42818	0.7904	0.7106	2.2066	0.9096	0.000963				
11	7	4.2331	5.1943	44.89962	0.8870	0.7752	2.2066	0.9096	0.00125				
12	7	3.3234	5.1943	38.02595	1.0016	0.8423	2.2066	0.9096	0.001603				
									Sum ring $h2_j$	6.9138E-03			
1	8	13.7708	5.1943	216.6148	0.3607	0.3529	2.2066	0.9096	0.000118		0.266502		
2	8	12.8611	5.1943	192.3894	0.3838	0.3745	2.2066	0.9096	0.000141		Sum of all calculus	2.720661	**0.340083**
3	8	11.9515	5.1943	169.819	0.4100	0.3986	2.2066	0.9096	0.00017				
4	8	11.0419	5.1943	148.9033	0.4397	0.4257	2.2066	0.9096	0.000207				
5	8	10.1322	5.1943	129.6426	0.4737	0.4562	2.2066	0.9096	0.000255				
6	8	9.2226	5.1943	112.0368	0.5129	0.4907	2.2066	0.9096	0.000317				
7	8	8.3129	5.1943	96.08579	0.5585	0.5299	2.2066	0.9096	0.000399				
8	8	7.4033	5.1943	81.7897	0.6118	0.5744	2.2066	0.9096	0.000508				
9	8	6.4937	5.1943	69.14849	0.6747	0.6246	2.2066	0.9096	0.000654				
10	8	5.5840	5.1943	58.16216	0.7493	0.6811	2.2066	0.9096	0.000848				
11	8	4.6744	5.1943	48.83071	0.8380	0.7433	2.2066	0.9096	0.001102				
12	8	3.7648	5.1943	41.15414	0.9436	0.8097	2.2066	0.9096	0.001424				
									Sum ring h_{1j}	6.1426E-03			
								Sum all rings h_{1j}		7.5456E-02			
										3.763181	**0.470398**		

Table 6. Calculations similar to Tables 4 and 5 using one, two, three, or four detector and source segments for h1 side of source only as described in text.

One source segment and one detector segment.													
1	1	6.7659	5.1943	72.75849	0.6547	0.6090	17.6528	10.0013	6.6611E-03	3.3221E-01	**0.67806**	0.60606	**0.28405**
Two source segments and one detector segment.													
1	1	9.2662	5.1943	112.8439	0.5109	0.4890	17.6528	5.0006	1.7243E-03		0.1816	0.1816	**0.1816**
2	1	4.2656	5.1943	45.1762	0.8833	0.7728	17.6528	5.0006	6.8073E-03				
									8.5317E-03	4.2550E-01	**0.42550**		
Two source segments and two detector segments.													
1	1	8.3836	5.1943	97.26529	0.5547	0.5267	8.8264	5.0006	2.1548E-03		0.2325		
2	1	3.3830	5.1943	38.42519	0.9935	0.8380	8.8264	5.0006	8.6780E-03				
								Sum ring h_{1j}	1.0833E-02	5.4026E-01			
1	2	10.1489	5.1943	129.9807	0.4731	0.4556	8.8264	5.0006	1.3948E-03		0.1423		
2	2	5.1483	5.1943	53.48536	0.7898	0.7102	8.8264	5.0006	5.2843E-03				
								Sum ring h_{1j}	6.6792E-03	3.3311E-01			
										8.7337E-01	**4.3668E-01**	0.3748	**0.18740**
Three source segments and three detector segments.													
1	1	8.9228	5.1943	106.5973	0.5272	0.5031	5.8843	3.3338	1.2521E-03		0.3560		
2	1	5.5891	5.1943	58.21833	0.7488	0.6808	5.8843	3.3338	3.1021E-03				
3	1	2.2553	5.1943	32.06717	1.1612	0.9173	5.8843	3.3338	7.5886E-03				
								Sum ring h_{1j}	1.1943E-02	5.9562E-01			
1	2	10.0997	5.1943	128.9842	0.4750	0.4574	5.8843	3.3338	9.4069E-04		0.2583		
2	2	6.7659	5.1943	72.75849	0.6547	0.6090	5.8843	3.3338	2.2204E-03				
3	2	3.4322	5.1943	38.76058	0.9869	0.8343	5.8843	3.3338	5.7104E-03				
								Sum ring h_{1j}	8.8714E-03	4.4244E-01			
1	3	11.2761	5.1943	154.131	0.4317	0.4184	5.8843	3.3338	7.2014E-04		0.1869		
2	3	7.9423	5.1943	90.06153	0.5792	0.5473	5.8842	3.3338	1.6123E-03				
3	3	4.6086	5.1943	48.21986	0.8451	0.7480	5.8843	3.3338	4.1154E-03				
								Sum ring h_{1j}	6.4478E-03	3.2157E-01			
									sum all segments	1.3596E+00	**4.5321E-01**	0.8012	**0.26705**

Table 6 (continued)
Four source segments and four detector segments.

1	1	9.1924	5.1943	111.4813	0.5143	0.4920	4.4132	2.5003	8.7803E-04		0.4286	
2	1	6.6921	5.1943	71.76504	0.6600	0.6132	4.4132	2.5003	1.7000E-03			
3	1	4.1918	5.1943	44.55189	0.8918	0.7782	4.4132	2.5003	3.4755E-03			
4	1	1.6915	5.1943	29.84186	1.2560	0.9509	4.4132	2.5003	6.3398E-03			
								Sum ring h_{1j}	1.2393E-02	6.1808E-01		
1	2	9.6337	5.1943	119.7898	0.4945	0.4746	4.4132	2.5003	7.8828E-04		0.3823	
2	2	7.1334	5.1943	77.86659	0.6294	0.5886	4.4132	2.5003	1.5041E-03			
3	2	4.6331	5.1943	48.44654	0.8424	0.7463	4.4132	2.5003	3.0649E-03			
4	2	2.1328	5.1943	31.52961	1.1812	0.9251	4.4132	2.5003	5.8376E-03			
								Sum ring h_{1j}	1.1195E-02	5.5832E-01		
1	3	10.5164	5.1943	137.5753	0.4588	0.4429	4.4132	2.5003	6.4047E-04		0.3014	
2	3	8.0161	5.1943	91.23831	0.5750	0.5438	4.4132	2.5003	1.1859E-03			
3	3	5.5158	5.1943	57.40446	0.7554	0.6856	4.4132	2.5003	2.3763E-03			
4	3	3.0155	5.1943	36.07373	1.0448	0.8648	4.4132	2.5003	4.7701E-03			
								Sum ring h_{1j}	8.9727E-03	4.4749E-01		
1	4	11.3990	5.1943	156.919	0.4276	0.4147	4.4132	2.5003	5.2577E-04		0.2367	
2	4	8.8987	5.1943	106.1682	0.5284	0.5041	4.4132	2.5003	9.4476E-04			
3	4	6.3984	5.1943	67.92051	0.6819	0.6303	4.4132	2.5003	1.8463E-03			
4	4	3.8981	5.1943	42.17598	0.9270	0.7998	4.4132	2.5003	3.7732E-03			
								Sum ring h_{1j}	7.0901E-03	3.5360E-01		
									sum all segments	1.9775E+00	**4.9438E-01**	1.3490 **0.33726**

References

1. R. A. Dewberry, S. R. Salaymeh, and T. B. Brown, **J. Radioanalytical and Nuclear Chemistry, vol 287,** No 1, (2011), January 2011.
2. R. A. Sigg, V. R. Casella, and R. A. Dewberry, "Nondestructive Assay Efficiency Calibration of HPGe Detectors for the ISOTOPIC Method", September 2005.
3. R. A. Dewberry, Invention Disclosure "Oven Source γ-PHA Acquisition Configuration", SRS-04-029, June 2004
4. R. A. Dewberry and F. S. Moore, "HEU Holdup Measurements in 321-M 'F' Out-gassing Oven Bank", WSRC-TR-2003-00408, January 2004.
5. R. A. Dewberry, S. R. Salaymeh, and F. S. Moore, "High Purity Germanium Assay of Uranium Storage Pigs for 321-M Facility," WSRC-TR-2001-00031, July 2001.
6. HEU Measurements of Holdup and Recovered Residue in the Deactivation and Decommissioning Activies of the 321-M Reactor Fuel Fabrication Facility at the Savannah River Site, R. A. Dewberry, S. R. Salaymeh, F. S. Moore, and V. R. Casella, **J**. **Radioanalytical and Nuclear Chemistry**, Vol 267, No. 3, March 2006.
7. S. R. Salaymeh and R. A. Dewberry, "HPGe Detector Efficiency Calibration Using HEU Standards," WSRC-TR-2000-000317, September 2000.
8. Private communication P. Santi to R. A. Dewberry 30 November 2010.
9. R. J. Haslett, Certificate of Calibration Source 50384-147, Analytics, June 1995.
10. R. A. Dewberry, Laboratory Notebook WSRC-NB-2006-00008, page 93.
11. V. R. Casella, R. A. Sigg, and R. A. Dewberry, "Nondestructive Assay Efficiency Calibration of the Pad19 MRS HpGe Detector, February 2006.
12. ISOTOPIC Version 2.0.6 Ametek/ ORTEC.
13. V. R. Casella and R. A. Dewberry, "Angular Dependence of Gamma Measurements Using a Shielded NaI Detector, WSRC-MS-2002-00073, 43rd Annual Conference of the Institute of Nuclear Material Management, Orlando, FA, July 2002.
14. D. J. Van Dalseur, Certificate of Calibration Gamma Standard Source 1278-38, Ho-166^{m}, December 2007.